Supplementary Materials of

"Pair production tomography enables imaging of MeV-scale gamma-emitting theranostic radionuclides"

GATE simulation material data

Below are the material data used for the GATE simulations in the .db file.

```
Water: d=1.00 g/cm3; n=2 ; state=liquid
        +el: name=Hydrogen   ; n=2
        +el: name=Oxygen     ; n=1

RibBone: d=1.92 g/cm3 ; n=11
        +el: name=Hydrogen   ; f=0.034
        +el: name=Carbon     ; f=0.155
        +el: name=Nitrogen   ; f=0.042
        +el: name=Oxygen     ; f=0.435
        +el: name=Sodium     ; f=0.001
        +el: name=Magnesium  ; f=0.002
        +el: name=Phosphor   ; f=0.103
        +el: name=Sulfur     ; f=0.003
        +el: name=Calcium    ; f=0.225

Lung:  d=0.26 g/cm3 ; n=9
        +el: name=Hydrogen   ; f=0.103
        +el: name=Carbon     ; f=0.105
        +el: name=Nitrogen   ; f=0.031
        +el: name=Oxygen     ; f=0.749
        +el: name=Sodium     ; f=0.002
        +el: name=Phosphor   ; f=0.002
        +el: name=Sulfur     ; f=0.003
        +el: name=Chlorine   ; f=0.003
        +el: name=Potassium  ; f=0.002

Adipose: d=0.92 g/cm3 ; n=11
        +el: name=Hydrogen  ; f=0.120
        +el: name=Carbon    ; f=0.640
        +el: name=Nitrogen  ; f=0.008
        +el: name=Oxygen    ; f=0.229
        +el: name=Phosphor  ; f=0.002
        +el: name=Calcium   ; f=0.001
```

Cube simulation extended methods and interpretation

All GATE cube simulations were conducted with the emstandard_opt3 physics list. List-mode tracking simulations in the phantom for e^+ KE and range quantification were conducted without

voxelization or range cuts. This simulation is computationally expensive, so to assess the source profile in the larger phantom in several materials, the GATE Production and Stopping actor was used with 0.1 mm range cuts and 0.5 mm voxelization.

Primary and secondary photon contributions to pair production

Supplementary **Figure S1** compares the electron and positron kinetic energies spectra for pair production initiated by the primary 2.617 MeV γ-ray and by secondary or subsequent photons. Direct interactions of the primary γ-ray accounted for 97.9% of all pair-production events, whereas the remaining 2.1% arose from secondary or later Compton/Bremsstrahlung photons.

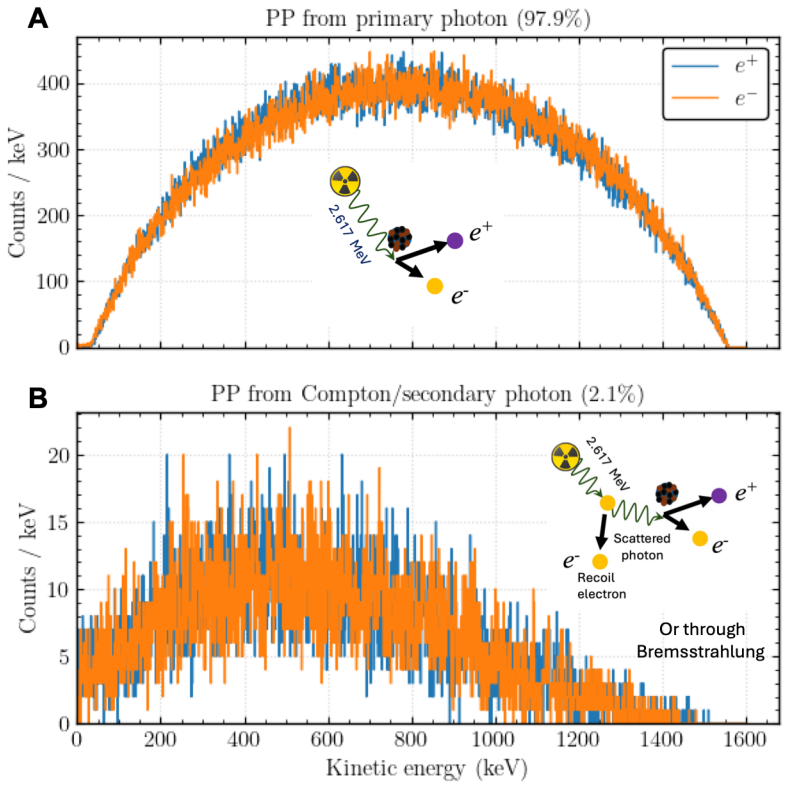


Figure S1. Electron and positron kinetic-energy distributions for pair-production events originating from (A) primary 2.617 MeV γ-rays and (B) secondary or later Compton/bremsstrahlung photons.

Localized pair-production and annihilation efficiencies of 20 cm cube

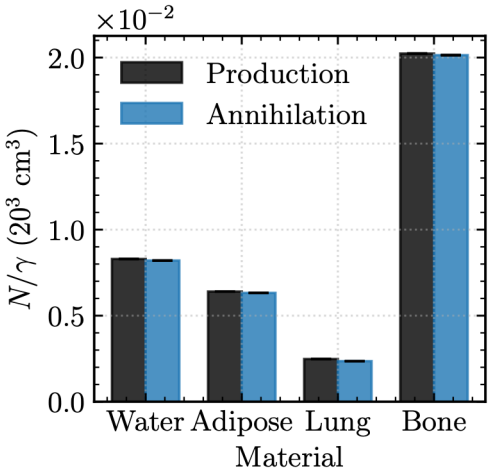


Figure S2. In the full cube simulation, nearly all produced positrons also annihilate in-phantom.

Simulation of heterogeneous tumor uptake

Additional simulations were performed of a 30-mm tumor with homogeneous and heterogeneous activity distributions. The heterogeneous model had higher uptake near the tumor periphery and lower uptake toward the center. Pair-production and annihilation-point distributions were compared using full projections, 5-mm slice projections, and 1D profiles as shown in **Figure S3** and **Figure S4**, respectively.

The heterogeneous tumor showed a modest reduction in the central region compared with the homogeneous distribution, indicating that uptake heterogeneity can be preserved to some extent in the PPT signal. However, visualization of small-size tumor heterogeneity in reconstructed images may be limited by spatial resolution, counting statistics, and reconstruction performance.

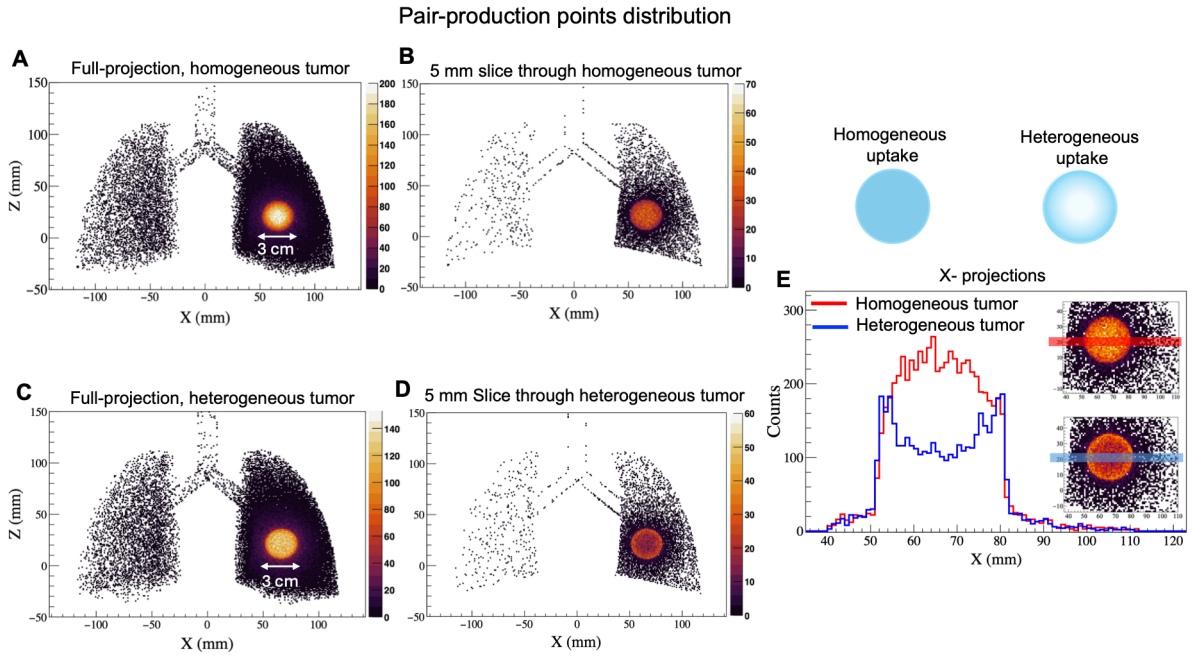


Figure S3. Pair-production event distributions for tumors with homogeneous and heterogeneous uptake. (A) Full projection and (B) 5-mm slice projection for homogeneous uptake. (C) Full projection and (D) 5-mm slice projection for heterogeneous uptake. (E) Corresponding one-dimensional line profiles comparing the homogeneous and heterogeneous uptake distributions.

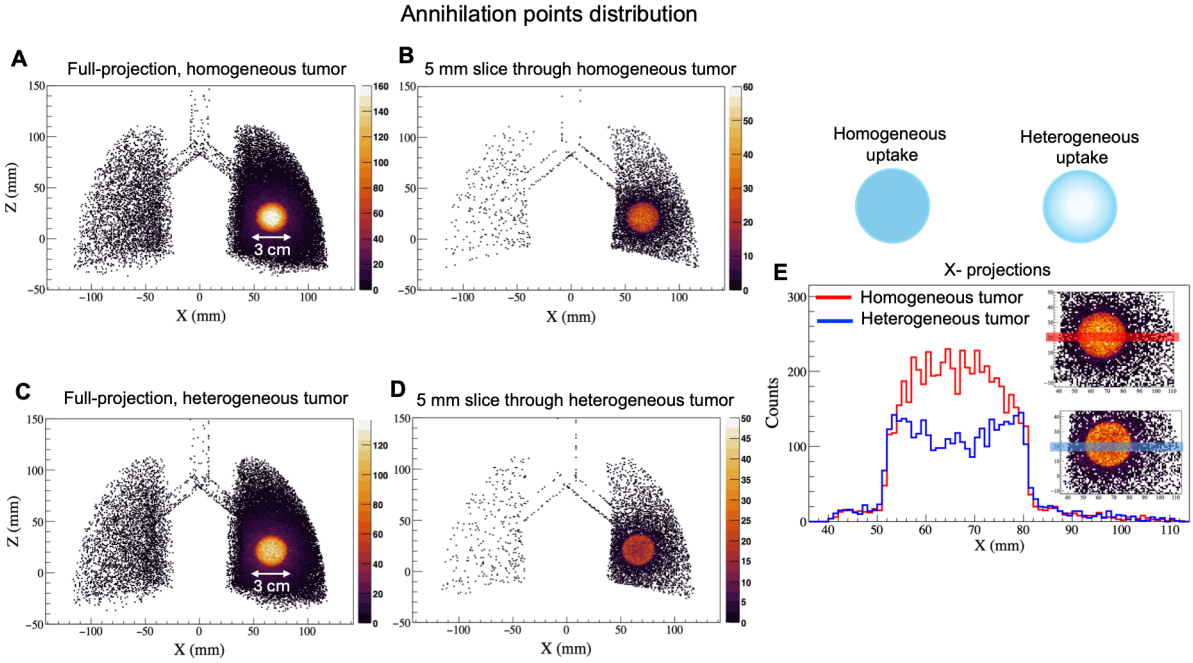


Figure S4. Annihilation points distributions for tumors with homogeneous and heterogeneous uptake. (A) Full projection and (B) 5-mm slice projection for homogeneous uptake. (C) Full projection and (D) 5-mm slice projection for heterogeneous uptake. (E) Corresponding one-dimensional line profiles comparing the homogeneous and heterogeneous uptake distributions.

Supplementary analysis of the effect of TOF information on PPT image quality

To provide an additional supportive demonstration of the benefit of TOF for PPT imaging, the same NU 4-2008 PET phantom was also scanned using the TOF Biograph Vision 600 PET/CT. The NanoScan system provides substantially higher spatial resolution (~0.7 mm) than the Biograph Vision 600 (~3–4 mm), whereas the Biograph Vision 600 provides TOF information with a coincidence timing resolution of ~214 ps. The side-by-side reconstructed PPT images obtained with two scanners are shown below in **Figure S5**.

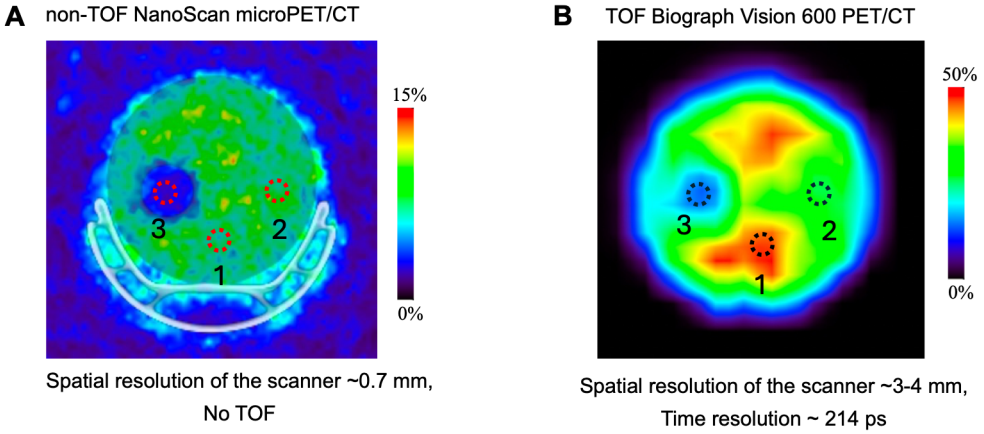


Figure S5. Reconstructed PPT images of NU 4-2008 PET phantom scanned with (A) the non-TOF NanoScan microPET/CT and (B) the TOF-enabled Biograph Vision 600 PET/CT.

Small regions of interest (ROI) were defined in the radioactive water, non-radioactive water, and air insert regions of the phantom. The ROI in the radioactive region was divided by that in the non-radioactive water and air regions to obtain radioactive-to-water and radioactive-to-air ROI ratios, respectively as shown in **Table S1**.

Table S1: Contrast ratios between the radioactive region and the non-radioactive air and water regions for TOF and non-TOF PPT images.

Ratio	**Non-TOF NanoScan**	**TOF Biograph Vision 600**
$\frac{ROI_1}{ROI_3} \equiv \frac{ROI_{Rad}}{ROI_{Air}}$	3.37	5.0
$\frac{ROI_1}{ROI_2} \equiv \frac{ROI_{Rad}}{ROI_{Water}}$	1.1	1.9

Despite the higher spatial resolution of the NanoScan system, the non-radioactive water region showed greater separation from the radioactive background in the Biograph Vision 600 image. Because the two systems differ in spatial resolution, sensitivity, detector geometry, and reconstruction methodology, this comparison was considered supportive rather than a direct assessment of the effect of TOF alone.